

# Improved Extended Kalman Filter Estimation Using Threshold Signal Detection With an MEMS Electrostatic Microscanner

Yi Chen D. Haijun Li, Zhen Qiu, Thomas D. Wang, and Kenn R. Oldham D. Member, IEEE

Abstract—In this paper, a threshold signal detector is proposed to improve the state estimation accuracy of an extended Kalman filter (EKF) and is validated experimentally with a microelectromechanical system electrostatic microscanner. A first-order derivative of Gaussian filter is used to detect and locate rapid changes in voltage signal caused by crossing of a threshold angle determined by maximum overlap of capacitive electrodes. The event-triggered measurement is used in the update step of the EKF to provide intermittent but more accurate angle measurements than those of the capacitive sensor's continuous output. Experiments on the electrostatic microscanner show that with the threshold signal detector incorporated; the average position estimation accuracy of the EKF is improved by 15.1% with largest improvement (30.3%) seen under low signalto-noise ratio conditions. A parametric study is conducted to examine sampling frequency and capacitance profile, among other factors that may affect detection error and EKF accuracy.

*Index Terms*—Kalman filter, microsensors, signal processing.

#### I. INTRODUCTION

APACITIVE sensing technology, commonly used in microelectromechanical system (MEMS) devices, has advantages of low-power operation, high sensitivity, and a relatively simple sensor structure compared to many other small-scale sensing mechanisms. The sensing principle is to measure the change of capacitance between two or more electrodes across a dielectric gap due to the change of gap geometry or the permittivity of the media between the gap.

Manuscript received July 26, 2018; revised January 16, 2019; accepted January 31, 2019. Date of publication March 4, 2019; date of current version September 30, 2019. This work was supported in part by Defense Advanced Research Projects Agency under Grant W31P4Q-12-1-0002, in part by the National Institutes of Health under Grant 5-R01-EB-020644, and in part by the National Science Foundation under Grant CMMI 1334340. (Corresponding author: Yi Chen.)

- Y. Chen and K. R. Oldham are with the Department of Mechanical Engineering, University of Michigan, Ann Arbor, MI 48109 USA (e-mail: davidsky@umich.edu; oldham@umich.edu).
- H. Li and T. D. Wang are with the Department of Biomedical Engineering, University of Michigan, Ann Arbor, MI 48109 USA (e-mail: haijunI@med.umich.edu; thomaswa@med.umich.edu).
- Z. Qiu is with the Department of Biomedical Engineering, Michigan State University, East Lansing, MI 48824 USA (e-mail: qiuzhen@msu.edu).

Color versions of one or more of the figures in this paper are available online at http://ieeexplore.ieee.org.

Digital Object Identifier 10.1109/TIE.2019.2901663

Various sensor geometries have been used in a vast array of sensing applications, such as measurement of short range distance (i.e., nanopositioning devices) [1], translational and rotational motion (i.e., MEMS inertial sensors) [2], [3], and pressure (i.e., microphone and pressure sensors) [4], [5].

One drawback of capacitive sensing is that its accuracy may be reduced by temperature and other environmental effects, which can cause undesired changes in geometric relations between electrodes [6], [7]. One potential solution is to find features of the sensing signal that correspond to specific positions that are both detectable and constant in the presence of unwanted geometric perturbations [8]. Such signal features can be used for measurement of threshold positions with high accuracy to "reset" position estimates and improve overall motion tracking accuracy. Design of capacitive sensors that generate threshold features can be intentional or a natural consequence of electrode geometry for a given application.

This paper introduces novel threshold signal detector realized with a derivative of Gaussian (DOG) function in the loop of an extended Kalman filter (EKF). It is intended to enhance the angular position and velocity estimation for MEMS microscanners. The paper explores factors impacting the performance of the estimation scheme, such as noise level, capacitance profile of the sensor, sampling rate.

Among prior research works, the idea of using threshold sensing to improve motion tracking can be found in [9], in which a sensor provided a measurement of the center mass of an MEMS accelerometer exceeding a threshold location; however, that literature did not discuss the realization of such a sensing mechanism. In [10], a design of an out-of-plane capacitive sensor using imbalanced capacitance to indicate threshold location was proposed; however, extraction of the signal was susceptible to drift of its capacitive signal. In [11], a Kalman filter estimation scheme with an asynchronized sensing scheme was proposed, in which a less accurate but frequently measured analog signal and a highly accurate but infrequent (twice per period of a waveform) threshold signal were used in a Kalman filter estimator. That work, however, again did not address the issue of how to extract the threshold signal and assumed perfect detection. Chen and Oldham [8] proposed using a DOG filter to detect threshold crossing signals and embedded its output as a more accurate source of measurement updates within a Kalman filter estimator. However, experimental results were not presented, and issues such as sampling rate and how to

0278-0046 © 2019 IEEE. Personal use is permitted, but republication/redistribution requires IEEE permission. See http://www.ieee.org/publications\_standards/publications/rights/index.html for more information.

fully incorporate a nonlinear capacitive sensor model were not addressed.

Given the limitations of previous works, it is desirable to study the factors that can affect the usage of threshold sensing in an EKF: How is the detection error distributed and can it be well modeled by normal distributions? What is the relationship between the variance of error and factors including sensor design (capacitance profile) and operating conditions (sampling rate, noise)? How should one pick suitable parameters for the DOG filter to optimize EKF performance?

This paper is organized as follows. Section II introduces some background on capacitive sensing, the DOG filter, and the EKF. Section III presents the process model, sensor model, and EKF implementation. Section IV presents the experimental setup. Section V presents the results of parametric studies of factors that can impact estimator performance. Section VI presents experimental results. Section VII concludes this paper.

#### II. PRELIMINARIES

# A. Capacitive Sensing Principles

Most capacitive sensors rely on a change in the geometric relationship between two electrodes to measure displacement. The two most common approaches are to vary the electrode gap or vary their overlapped area [2]. In microscale devices, gap variation typically provides more sensitivity, at the cost of nonlinearity and a limited range of measurement. Change in area typically provides less sensitivity but more linear behavior, and may be designed to provide a unique feature of a maximal capacitance when electrodes reach their maximum overlapped area. We will examine a method to use such a geometric feature to generate and extract a threshold measurement that enhances accuracy of motion estimation by an EKF, and experimentally validate the method with an MEMS microscanner.

# B. Electrostatic Microscanner and Threshold Sensing

The sample device studied in this paper, shown in Fig. 1(a), is an electrostatically driven dual-axis microscanner. It includes two reflective mirror surfaces for dual axes confocal imaging and multiple groups of comb fingers. Each group of comb fingers consists of a moveable comb and a fixed comb [see Fig. 1(b)]. By applying driving voltage with a carefully selected frequency, the comb finger can generate electrostatic torque that produces parametric resonance in the form of tilting motion with a frequency half that of the driving voltage [12].

This class of microscanner is designed to deflect light for imaging purposes [13]. While the comb-fingers are designed to serve as actuators, they can also serve as capacitive sensors to measure the tilting angles of the mirror. The capacitance of the comb finger as a function of tilting angle [14] is

$$C_{s}\left(\theta\right) = \frac{\epsilon_{0}\epsilon_{r}nA\left(\theta\right)}{D}\tag{1}$$

where  $\varepsilon_r$  is the relative static permittivity (1 for air),  $\varepsilon_0$  is the dielectric constant (8.8542  $\times$  10<sup>-12</sup> Fm<sup>-1</sup>), A is the overlap area of electrodes, D is the distance between the electrodes,  $C_s(\theta)$  is sensing capacitance,  $A(\theta)$  is the total area of overlap between the comb fingers as a function of tilting angle  $\theta$ , and n is the

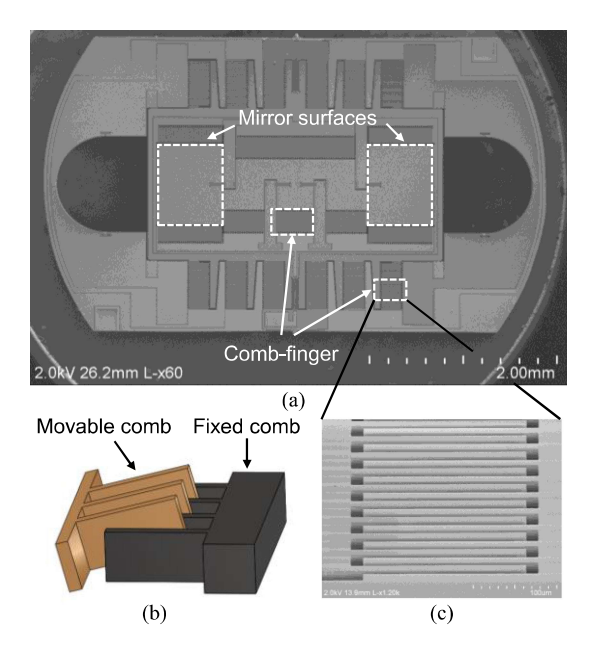


Fig. 1. (a) Scanning electron microscope image of a parametrically resonant microscanner tested in this paper. (b) Illustration of comb-finger electrodes used as actuators and capacitive sensors. (c) Zoomed in image of a representative comb-finger structure.

number of pairs of comb fingers. The capacitance reaches its maximum when the overlapped area is maximized.

To transduce the capacitance change into measurable voltage signal, we employ a sensing circuit that applies constant bias voltage  $V_{\rm bias}$  at the sensing electrodes. The change of capacitance can be converted to a sensing current that is amplified by a feedback resistance  $R_s$  and transimpedance amplifier into an analog voltage signal  $y_{\rm cap}$  by

$$y_{\text{cap}} = -R_s V_{\text{bias}} \frac{dC_s(\theta)}{dt}.$$
 (2)

It is worth noting that other types of sensing circuits can be applied [15]. Amplitude modulation and demodulation is commonly used to separate and suppress any feedthrough disturbance introduced by parasitic capacitance in the sensing electrodes, coupling them to the device's driving voltage. However, modulation and demodulation introduces undesired delays and skew in the filtered signal, which will negatively impact threshold measurement in terms of reducing its accuracy. In this paper, since the focus is on validating the concept of generating and extracting threshold angle measurements and evaluating their effectiveness in an EKF framework, the transimpedance approach is used. This realization is also beneficial for implementation using very few electrical interconnects in a compact space, such as an endomicroscope. To compensate for feedthrough, later experiments were performed with a power cutoff strategy, discussed in Section IV.

For this device, capacitance reaches its maximum value when the movable comb fingers cross the mirror's central position and fully overlap the fixed comb fingers. With the transimpedance circuit, a rapid change in sign and magnitude of the output sensing signal occurs, as illustrated in Fig. 2(a)–(d). This is referred to as the threshold angle for this system.

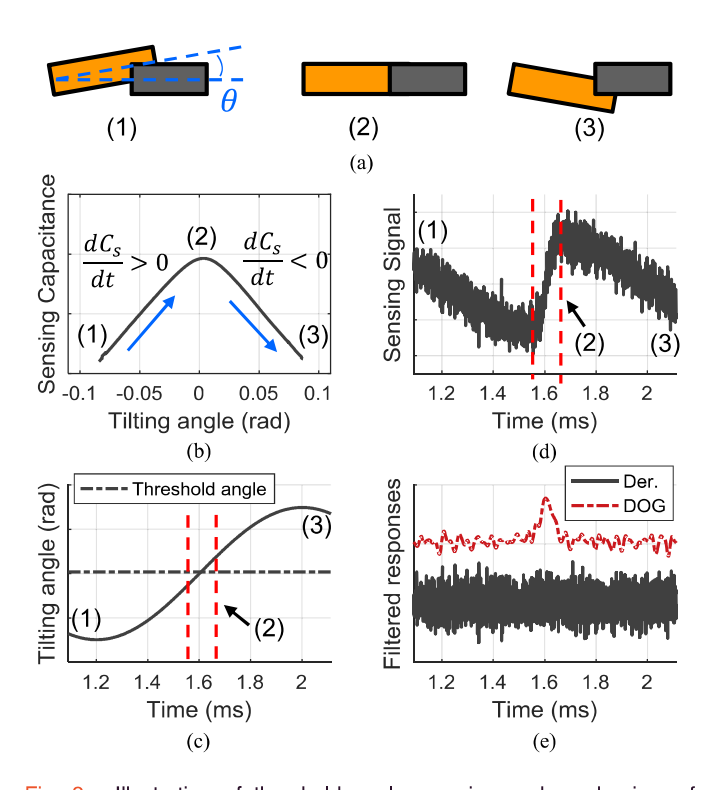


Fig. 2. Illustration of threshold angle crossing and mechanism of threshold angle sensing and detection. (a) Configurations of comb finger (1)–(3) correspond to before, at, and after threshold angle crossing, respectively. (b) Sensing capacitance versus tilting angle  $\theta$ . (c) Tilting angle versus time. (d) Noisy sensing signal versus time; the crossing event generates rapid change of signal around (2). (e) Comparison of filtered signal by a derivative operator and a DOG operator. DOG operator is effective in detecting the timing of rapid signal change.

Knowing the exact timing of the threshold angle crossing is beneficial in high-accuracy estimation of the angular position at that time. However, in practice, it can be challenging to determine the threshold-crossing time from the measured signal due to noise and bias. Since the threshold position crossing corresponds to a locally maximum rate of change of voltage, it might be obvious to adopt a derivative operator as a first attempt to retrieve crossing information. However, as illustrated in Fig. 2(e), taking the derivative of a noisy signal does not necessarily provide a reliable outcome. To resolve this issue, a first-order DOG filter is proposed to extract the timing of the threshold position crossing [8]. A DOG filter is used as an approximated optimal filter for edge detection in the field of computer vision [16] and has merits of good detection (low probability of false detection), good localization (low variance of detection error), and one response to a single edge (one maximum or minimum corresponds to one crossing) [17].

While the introduction of a DOG filter provides an efficient and convenient realization for detecting threshold crossing timing, detection accuracy is still not perfect. In the presence of noise, the detected timing can deviate from the true timing. According to Canny [17], for the detection error in timing for a one-dimensional step edge  $e_{t,\rm th}$  its variance  $R_{t,\rm th}$  is expressed as

$$R_{t,\text{th}} = E \left[ e_{t,\text{th}}^2 \right] = \frac{\sigma_n^2 \int_{-w}^w \dot{f}(\tau)^2 d\tau}{\left[ \int_{-w}^w \dot{f}(\tau) \dot{y}(-\tau) d\tau \right]^2}$$
(3)

where  $f(\tau)$  is the filter for edge detection,  $y(\tau)$  is the signal including the edge,  $\tau$  is a dummy variable, and  $\sigma_n$  is the standard deviation of the normally distributed zero mean additive noise to the sensing signal. This expression reveals that  $R_{t,\mathrm{th}}$  is proportional to the variance of noise (the noisier the signal, the less accurate the detection) and inversely proportional to the edge's slope (the sharper the slope, the more accurate the detection).  $R_{t,\mathrm{th}}$  is a key factor in threshold-sensing performance and can be used to derive the error covariance matrix needed to obtain optimal state estimates with an EKF.

# C. Challenges

To carry out the EKF algorithm using threshold sensing information, a value for  $R_{t,\,\,\mathrm{th}}$  is needed. Although (3) gives a theoretical derivation, in operation, it is difficult to obtain a signal y(t) containing an edge that is uncorrupted by noise. Hence, it is desirable to estimate  $R_{t,\,\mathrm{th}}$  offline, which leads to several issues. First, the EKF assumes the process is subjected to normally distributed noise. We will investigate the distribution of  $e_{t,\,\mathrm{th}}$ , and more importantly, the distribution of detection error of threshold angle  $e_{\theta,\,\mathrm{th}}$  to ensure that the EKF can be appropriately applied. Second, the expression of  $R_{t,\,\mathrm{th}}$  in (3) is derived in continuous time and does not take sampling effects into account. Since the EKF is implemented in discrete time, the choice of sampling rate can impact estimation performance.

#### III. SYSTEM MODELING

In this section, the process model, sensor model, and EKF incorporated with threshold sensing are described.

#### A. Process and Sensor Model

The dynamics of the tilting motion of the microscanner are modeled as a second-order, nonlinear time invariant system

$$J\ddot{\theta} + b_v \dot{\theta} + k_s \theta = \tau \left( \theta, V_{\rm dr} \right) \tag{4}$$

where J is the moment of inertia of the microscanner,  $b_v$  is the damping coefficient, and  $k_s$  is the spring constant of a torsional spring. The torsional load generated by the comb finger  $\tau_L$  is

$$\tau_L (\theta, U) = \frac{1}{2} \frac{dC_{\rm dr}}{d\theta} V_{\rm dr}^2$$
 (5)

where  $V_{\rm dr}$  is the driving voltage, and  $C_{\rm dr}$  is the driving capacitance formed by the comb fingers that generate tilting motion. Let  $\boldsymbol{X} = [x_1 \ x_2]^T$  to be state vector, where  $x_1 = \theta$  and  $x_2 = \dot{\theta} = \omega$  is the tilting angular velocity. Letting  $\omega_n = \sqrt{k_s/J}$ ,  $\zeta = \frac{b_v}{2\sqrt{Jk_s}}$ , where  $\omega_n$  is the natural frequency of the tilting mode and  $\zeta$  is the damping ratio. Equation (4) becomes

$$\dot{\mathbf{X}} = \begin{bmatrix} 0 & 1 \\ -\omega_n^2 & -2\zeta\omega_n \end{bmatrix} \mathbf{X} + \frac{1}{2} \frac{dC_{\mathrm{dr}}}{dx_1} V_{\mathrm{dr}}^2.$$
 (6)

Denoting the sampling interval to be  $T_s$ , and assuming that the process is subject to zero-mean, normally distributed process noise, the discretized process model for the EKF becomes

$$\boldsymbol{X}_{k} = g\left(\boldsymbol{X}_{k-1}, V_{dr,k}\right) + \boldsymbol{v}_{k} \tag{7}$$

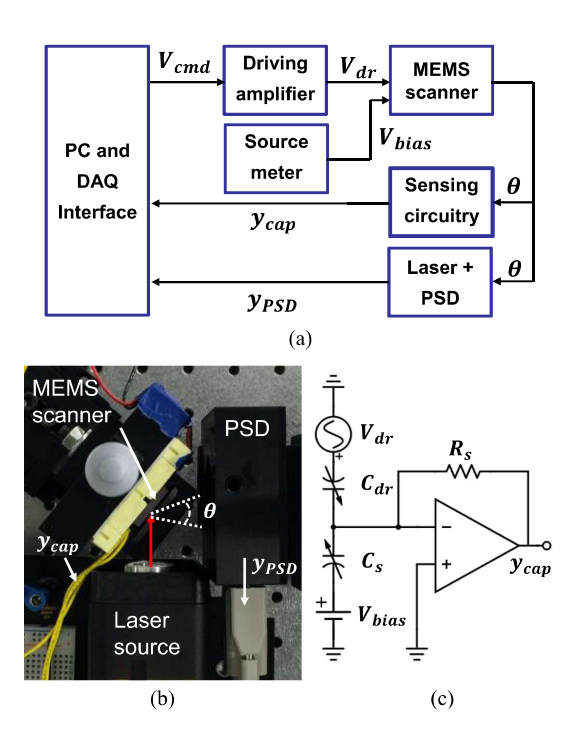


Fig. 3. Experimental setup. (a) Schematic of major experimental modules and signal flow. (b) Top view of setup and illustration of geometric relationship between the laser source, MEMS scanner, and PSD. (c) Schematic sensing and driving circuitry for the MEMS scanner.

where  $g(\cdot)$  is defined as

$$g\left(\boldsymbol{X}_{k-1}, V_{\mathrm{dr},k}\right) = \begin{bmatrix} 1 & T_{s} \\ -\frac{k_{s}}{J}T_{s} & 1 - \frac{b_{v}}{J}T_{s} \end{bmatrix}$$
$$\boldsymbol{X}_{k-1} + \begin{bmatrix} 0 \\ \frac{T_{s}}{2J} \end{bmatrix} \frac{dC_{\mathrm{dr}}}{dx_{1}} \left(k\right) V_{\mathrm{dr},k}^{2}. \tag{8}$$

For the sensor model, (2) shows that the signal from a capacitive sensor with current-based readout [see Fig. 3(c)] is proportional to the rate of change of capacitance  $dC_s/dt$ . Since  $\frac{dC_s}{dt} = \frac{dC_s}{d\theta} \frac{d\theta}{dt}$ , where  $\frac{dC_s}{d\theta}$  is the rate change of capacitance with respect to tilting angle  $\theta$ . Denoting  $\frac{d\theta}{dt} = \omega$ , we have a measurement used by the EKF  $y_{\rm cap}$  of

$$y_{\rm cap} = \left[ -R_s V_{\rm bias} \frac{dC_s}{d\theta} \right] \omega = h_{\rm cap} (\theta) \omega$$
 (9)

where  $h_{\rm cap}(\theta)=-R_sV_{\rm bias}\frac{dC_s}{d\theta}$  is  $\theta$ -dependent sensor gain,  $R_s$  is a constant resistance, and  $V_{\rm bias}$  is a constant bias voltage.

# B. EKF With Threshold Sensing

The proposed EKF includes a hybrid-sensing scheme where the signal of the capacitive sensor is regarded as a normal analog measurement, and the detection of threshold crossing is applied intermittently. The procedure for applying the EKF with the fusion of the two types of measurements is provided in Table I. In Table I,  $\hat{X}_k^-$  is the *a priori* state estimates at the *k*th step,  $P_k^-$  is the *a priori* error covariance matrix at the *k*th step,  $P_{k-1}$  is the *a posteriori* error covariance matrix at the (k-1)th step,

TABLE I

ALGORITHM, EKF WITH HYBRID SENSING SCHEME

1. Project *a priori* state estimates

$$\widehat{X}_{k}^{-} = g(\widehat{X}_{k-1}, V_{dr,k}); \quad P_{k}^{-} = G_{k}P_{k-1}G_{k}^{T} + Q$$

2. Update matrix of observation

If threshold detection is negative

$$\widehat{Y}_k = [0 \ h_{cap}(\widehat{\theta}_k^-)] \widehat{X}_k^- = H_k \widehat{X}_k^-; \quad R = R_{cap}$$

If threshold detection is positive

$$\widehat{\boldsymbol{Y}}_{k} = \begin{bmatrix} 1 & 0 \\ 0 & h_{cap}(\widehat{\boldsymbol{\theta}_{k}^{-}}) \end{bmatrix} \widehat{\boldsymbol{X}_{k}^{-}} = \boldsymbol{H_{k}} \widehat{\boldsymbol{X}_{k}^{-}}; \quad \boldsymbol{R} = \begin{bmatrix} R_{\theta,th} & 0 \\ 0 & R_{cap} \end{bmatrix}$$

3. Compute EKF gain with threshold sensing

$$K_k = P_k^- H_k^T (H_k P_k^- H_k^T + R)^{-1}$$

4. Update *a posteriori* state estimates

$$\widehat{X}_k = \widehat{X}_k^- + K_k (Y_k - \widehat{Y}_k); \quad P_k = P_k^- - K_k H_k^T P_k^-$$

Q is the covariance matrix of process noise, and  $G_k = \frac{\partial g}{\partial X_{k-1}}$  is the Jacobian of the process model.

Depending on whether a threshold detection is positive, the form of the matrix of observation  $\boldsymbol{H}_{k}$ , the estimated sensing signal  $\hat{Y}_{k}$  and the covariance matrix of measurement noise  $\boldsymbol{R}$  will vary.  $R_{\text{cap}}$  is the measurement noise variance for the analog capacitance signal and  $R_{\theta,\text{th}}$  is the variance of  $e_{\theta,\text{th}}$ . The Kalman gain  $\boldsymbol{K}_{k}$  is then computed and a posteriori state estimates  $\hat{\boldsymbol{X}}_{k}$  and a posteriori estimate error covariance matrix  $P_{k}$  are finally updated with the measurement at the kth step  $Y_{k}$ . Measurement  $\boldsymbol{Y}_{k} = [\theta_{\text{th}} \ y_{\text{cap},\ k}]^{T}$  is for positive detection and  $\boldsymbol{Y}_{k} = y_{\text{cap},\ k}$  is for negative detection.

#### IV. EXPERIMENTS AND MODEL IDENTIFICATION

An experimental testbed was prepared and used to identify parameters of the process and sensor models, and to verify the effectiveness of the DOG filter in threshold-crossing detection and the EKF using the hybrid-sensing scheme.

#### A. Experimental Setup and Methods

As depicted in Fig. 3(a), computer-generated voltage commands were transmitted to an NI PCIe 6251 DAQ with sampling rate of 500 kHz. The voltage command was amplified by a TEGAM 2340 amplifier with 20 times amplification, and the amplified driving voltage fed to the MEMS scanner to generate tilting motions. Tilting motion was measured by two means: reflection of a laser by the scanner and conversion of the capacitive sensing current as described in (9).

Laser tracking is treated as the ground truth of tilting motion. Fig. 3(b) shows the geometric relation between the MEMS scanner mounted on a dual inline package, a JDSU 1500 heliumneon laser source, and an On-Trak 1L10 position-sensing detector (PSD). The laser beam is emitted by the source, reflected by the scanner's mirror surface, and received by the PSD, amplified by an On-Trak-301SL sensing amplifier.

On-chip sensing is used by the EKF. Fig. 3(c) depicts the schematic of integrated driving and sensing circuitry. An acdriving voltage is fed into comb fingers used for driving, and a

dc bias voltage provided by a source meter  $V_{\rm bias}$  is fed into comb fingers used for sensing. The generated current flow through the shared grounding terminal is fed into a sensing circuit, which consists of a TI OPA2140 amplifier with a feedback resistance of  $10~{\rm M}\Omega$ .

Since the objective of this paper is to validate the method of using a DOG filter for threshold angle-crossing detection and EKF integration, it is useful to eliminate the potential disturbances introduced by feedthrough of the driving voltage. Therefore, during experiments, a power cutoff method was applied. A 0–60 V periodic  $V_{\rm dr}$  was applied to the MEMS scanner, and the frequency was swept from 1600 to 1220 Hz to reach a maximized amplitude of tilting motion, given electrostatic spring softening [18]. Once the tilting motion was stabilized  $V_{dr}$  was set to zero, while  $V_{\rm bias}$  was maintained at a constant 10 V. Such a sequence of voltage commands allows the microscanner to freely oscillate briefly after the power cutoff, and the sensing current induced by the oscillation can be amplified and recorded without feedthrough disturbance.

A total of ten trials of power cutoff experiments were performed and  $V_{\rm dr}, y_{\rm cap}$ , and  $y_{\rm PSD}$  were recorded at 500-kHz rate. The data were postprocessed as follows for consistency: Each time series was truncated at the power cutoff and 80 ms afterward (approximately 50 periods of free oscillation). The delay between PSD measurement and sensing circuit measurement was experimentally calibrated to be 0.114 ms.

To detect a threshold crossing, a DOG filter is applied to the sensing signal using the *nlfilter* function in MATLAB, which is a general sliding-neighborhood operation. The filtered signal is then processed with nonmaximum suppression to suppress the filtered response except the local maxima, and these local maxima are then extracted to indicate the detected threshold crossing. In this paper, the threshold detections are extracted in a postprocessing fashion. To achieve a near real-time threshold detection, a buffer can be used to store measurements from past to present, and DOG filter can be applied to the signal in the buffer to generate a local maximum for threshold detection.

#### B. Identification of Process and Sensor Models

The tilting angle measured by the PSD,  $\theta_{PSD}$  is computed as

$$\theta_{\rm PSD} = \arctan\left(\frac{y_{\rm PSD}G_{\rm PSD}}{L_m}\right)$$
 (10)

where  $G_{\rm PSD}(0.5~{\rm mm/}V)$  is the gain of the PSD-sensing amplifier and  $L_m$  is the distance from the scanner surface to PSD surface and is measured to be 32.7 mm. A representative trajectory of the system is shown Fig. 4(a); by fitting the decay curve using linear viscous damping [19],  $\omega_n$  and  $\zeta$  were identified to be 624.6 Hz and 0.0066, respectively.

The sensor model is the sensing capacitance as a nonlinear function of angle  $C_s(\theta)$ , which can be experimentally identified by mapping the trajectory  $C_s(t)$  versus  $\theta_{\rm PSD}(t)$  in various experiments. First,  $C_s(t)$  is obtained by integrating  $y_{\rm cap}$  with respect to time, from (2)

$$C_s(t) = \int_{t_0}^{t_f} -R_s V_{\text{bias}} y_{\text{cap}} dt$$
 (11)

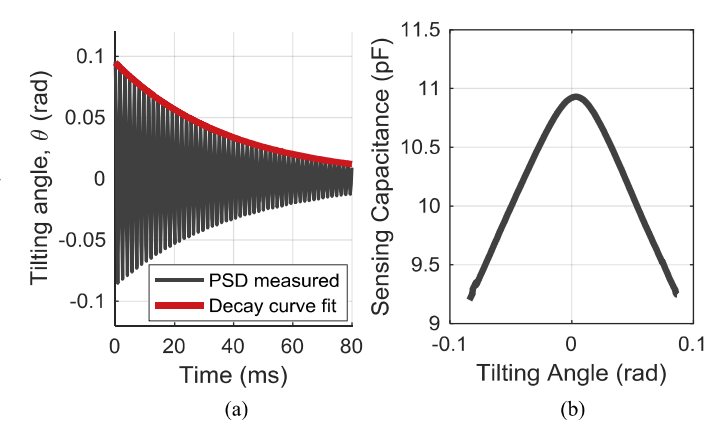


Fig. 4. (a) Experimentally measured free oscillations versus simulated decay curve of free oscillations with identified natural frequency and damping ratio of the MEMS scanner. (b) Experimentally identified sensing capacitance with respect to tilting angle.

TABLE II
BASE SETTING FOR PARAMETRIC STUDY

Symbol	Description	Value	
$f_{s}$	sampling frequency	500 kHz	
$\theta_{amp}$	amplitude of $\theta$	0.15 rad	
$f_m$	motion frequency	625 Hz	
$\sigma_n$	standard deviation of noise	0.0435 V	
$R_s$	feedback resistance	$10 \mathrm{M}\Omega$	
$V_{bias}$	bias voltage	10 V	
$W_{DOG}$	width of DOG filter	400	
$\sigma_{DOG}$	standard deviation of DOG filter	15	

Using the corresponding  $\theta_{\rm PSD}(t)$ , one can establish the mapping of  $C_s(\theta)$  and  $\frac{dC_s}{d\theta}(\theta)$  and, therefore, compute  $h_{\rm cap}(\theta)$  as suggested in (9). Fig. 4(b) shows the identified sensor gain function  $h_{\rm cap}(\theta)$ . The capacitance profile can be approximated by a Gaussian model [14].

The threshold location  $\theta_{\rm th}$  is identified by computing the average angular displacement at which the peak capacitance is reached among the experimental measurements. Nominally,  $\theta_{\rm th}$  should be zero for the planar microscanner geometry, but in practice a nonzero value may occur due to finite fabrication tolerance of electrodes and residual stresses. In this device,  $\theta_{\rm th}$  was calibrated to be 0.0037 rad.

# V. PARAMETRIC STUDY OF FACTORS IMPACTING THRESHOLD DETECTION

In this section, parametric studies investigate the properties of the error of threshold detection and some contributing factors, including the sensor map and sampling rate. A sinusoidal tilting motion is simulated within the capacitive sensor model described by (9), with additive, zero-mean normally distributed measurement noise. The signal generated by the capacitive sensing model is passed into a DOG filter to compute the detection error in timing  $e_{t,th}$  and detection error in threshold angle  $e_{\theta,th}$ . Baseline settings from experimental device identification are summarized in Table II.

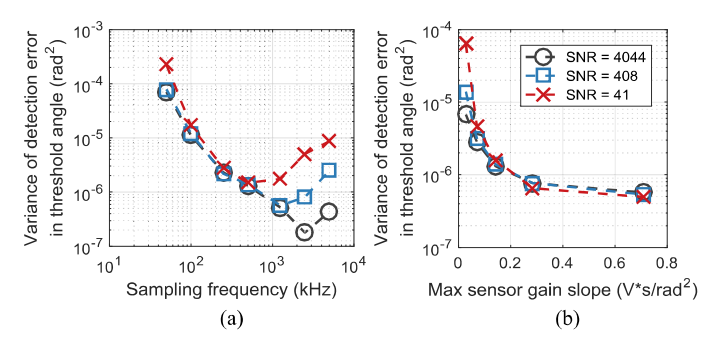


Fig. 5. (a) Variance of detection error in threshold angle versus sampling frequency. (b) Variance of detection error in threshold angle versus maximum sensor gain slope.

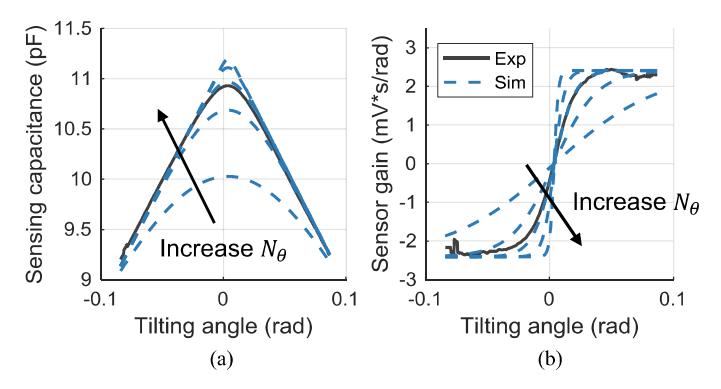


Fig. 6. Sweep of maximum sensor gain slope. (a) Sensing capacitance becomes sharper around threshold angle as  $N_{\theta}$  increase. (b) Sensor gain slope becomes steeper around threshold angle as  $N_{\theta}$  increases.

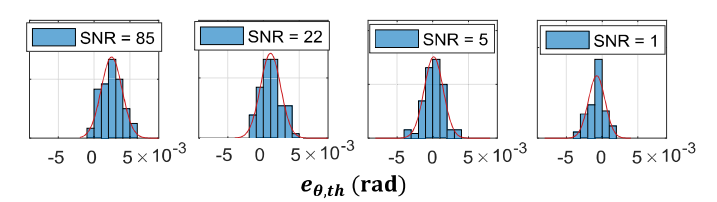


Fig. 7. Distribution of detection errors in threshold angle from experimental measurements at different SNRs can be well modeled by normal distributions.

#### A. Sampling Rate Effects

In (3), sampling rate is not singled out as a factor that affects the detection of threshold signal. However, this is not the case during digital implementation, as a low sampling rate introduces quantization error and a high sampling rate may allow excessive sensor noise into the filtering process. Therefore, a series of simulations was conducted, from the baseline in Table II, and the sampling rate was swept from 50 kHz to 5 MHz. The filter size was adjusted proportionally to maintain a fixed ratio between the filter size and the period of the waveform. The SNR was also varied by multiplying  $\sigma_n$  by factors of 0.1 and 10.

The simulation result is shown in Fig. 5(a). The result shows that  $R_{t,\rm th}$  increases as the sampling rate is slower than 1250 kHz, which is mainly due to quantization noise. As the sampling rate increases,  $R_{t,\rm th}$  increases, attributed to noisier samples being taken into the filtering process. This suggest that an optimal selection for sampling frequency for a given threshold sensor

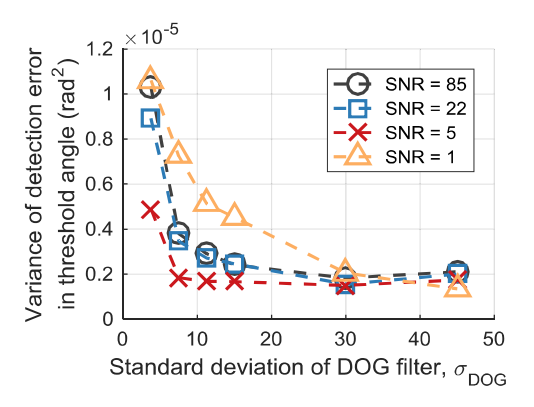


Fig. 8. Variance of detection error in threshold angle during experiments with respect to the standard deviation of the DOG filter.

exists, and one can properly size the data acquisition system to achieve the lowest variance of detection timing error without overreaching for fast sampling capability.

#### B. Sensor Map Effects

Equation (3) suggests that the variance of detection timing error is inversely proportional to the rate of change of the signal  $\dot{y}(t)$ , meaning that a sharper and more abrupt change of signal amplitude can be more accurately located in a statistical sense. To test the significance of the change, one way is to change the capacitance profile formed by the electrodes. More specifically, we are interested in  $dC_s/d\theta$  around threshold location, as higher values will prompt higher  $\dot{y}_{\rm cap}(t)$  as suggested in (9). In this paper, a modified logistic function is used to generate a modeled sensor gain,  $\hat{h}_{\rm cap}$  as

$$\hat{h}_{\text{cap}}(\theta) = N_g \left( \frac{1}{1 + e^{-N_{\theta}\theta}} - 0.5 \right)$$
 (12)

where  $N_g$  is the normalization factor for gain, and  $N_\theta$  is the normalization factor for angle. The modeled sensing capacitance simply takes the integration of  $\hat{h}_{\rm cap}(\theta)$  with respect to tilting angle

$$\hat{C}_s(\theta) = -\frac{1}{R_s V_{\text{bias}}} \int_{\theta_{\text{max}}}^{\theta_{\text{max}}} \hat{h}_{\text{cap}}(\theta) d\theta.$$
 (13)

By sweeping  $N_{\theta}$ , one can vary the maximum sensor gain at the vicinity of threshold location, with larger  $N_{\theta}$  corresponding to steeper slop and more drastic change of capacitance at  $\theta_{\rm th}$ , as depicted in Fig. 6. The experimentally identified sensor gain was used as baseline to generate a series of sensor model with  $N_{\theta}$  swept from 0.2 to 5.

Fig. 5(b) shows the simulation results. We find that  $R_{t,\rm th}$  decreases as expected as the maximum sensor gain slope increases. The significance of this change is comparable at various sensor noise densities.

# VI. EXPERIMENTAL RESULTS

In this section, experimental results are presented to evaluate the effect of different DOG filters on threshold detection and EKF performance. The decaying tilting motion of the

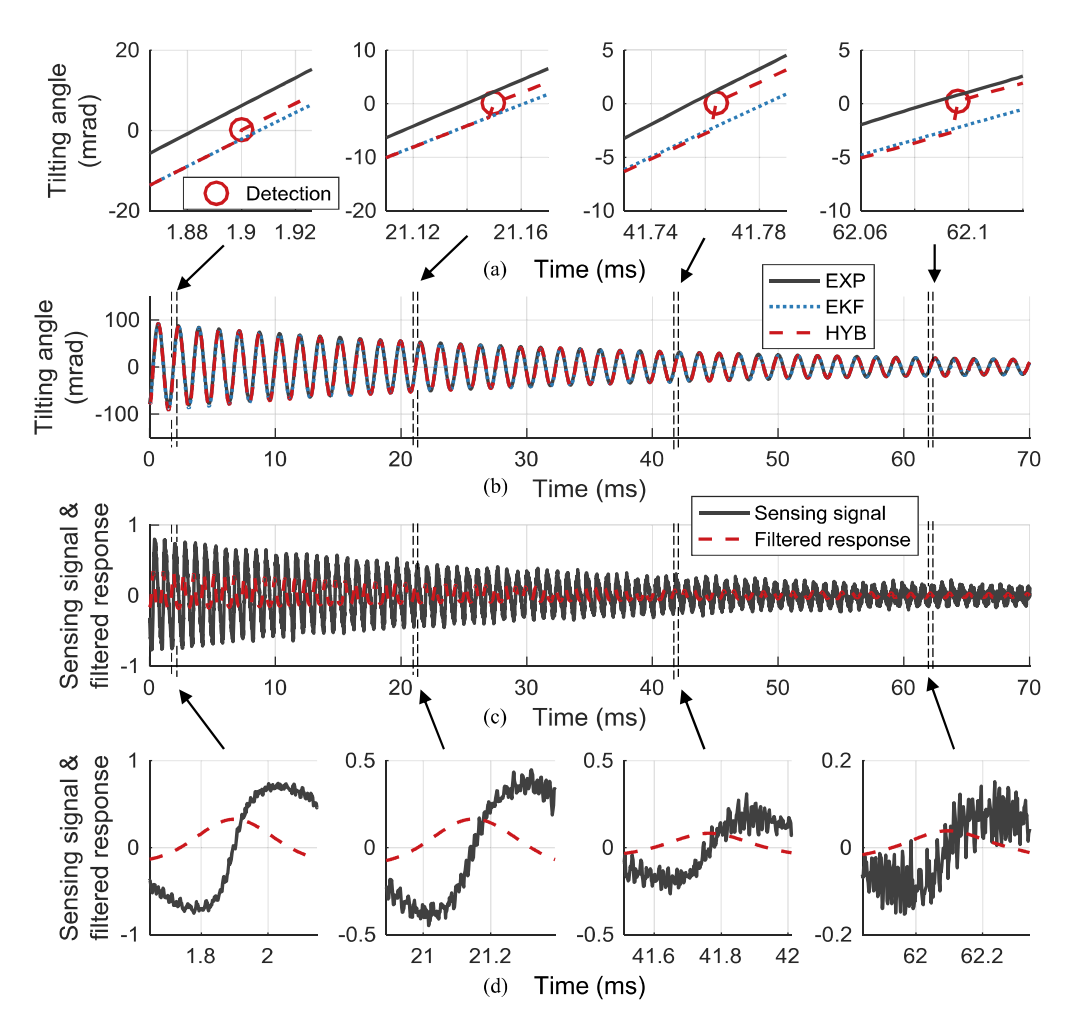


Fig. 9. Representative experimental measurement and estimation result in time domain. (a) Four snapshots of threshold angle crossing detection improving tilting angle estimation. (b) Overall trajectories of tilting angle measurement and estimations. (c) Overall trajectories of sensing signal and response of the DOG filter. (d) Corresponding snapshots of sensing signal, where local maxima of filtered response detects threshold angle crossing.

microscanner after power cutoff provides an opportunity to vary SNR by segmenting trajectories. Therefore, for each trial, the measurements and estimated states are divided into four segments, with SNR ranging from 85 to 1. For conciseness, the EKF using the hybrid sensing scheme of capacitive analog sensing and threshold sensing is abbreviated as HYB.

#### A. Effect of DOG Filter on Threshold Detection

The EKF implementation assumes that process noise and measurement noise are normally distributed. Therefore, it is helpful to verify the distribution of measurement noise of the threshold sensor. Threshold angle measurement noise is defined as the error between the threshold angle and the ground truth angle at the instant of detection, denoted as  $e_{\theta,\rm th}$ . Here,  $e_{t,\rm th}$  and  $e_{\theta,\rm th}$  are computed by taking the differences between the timing and angle at the detected threshold crossing and their ground truth values, respectively. The distribution of  $e_{t,\rm th}$  and  $e_{\theta,\rm th}$  computed from experimental measurements was analyzed using the Kolmogorov–Smirnov test [20]. Results indicate that the error distribution can be well modeled by normal distributions at the tested conditions, shown in Fig. 7.

Different settings for the DOG filter were also applied to  $y_{\rm cap}$  and the EKF to evaluate their impact on the variance of  $e_{\theta,\rm th}$  and accuracy of state estimation. The filter size  $w_{\rm DOG}$  was swept from 80 sample points to 400 sample points and  $\sigma_{\rm DOG}$  was swept from 1.5 to 45. No significant performance variation was found in varying  $w_{\rm DOG}$  while keeping  $\sigma_{\rm DOG}$  the same. However, as shown in Fig. 8, the variance of  $e_{\theta,\rm th}$  varies as  $\sigma_{\rm DOG}$  varies for all four cases, which suggests a large  $\sigma_{\rm DOG}$  is beneficial in reducing overall error variance.

#### B. Effect of Threshold Sensing on EKF

A representative estimation result is depicted in Fig. 9. The ground truth (EXP) and estimated tilting motion (EKF and HYB) are shown.

Fig. 9(a) shows the change in estimator output with the introduction of threshold crossing detection:  $\hat{\theta}$  by HYB is corrected at the instant of threshold crossing detection and, therefore, is closer to the ground truth value. Fig. 9(d) shows that the local maxima of the DOG filter response corresponds to the vicinity of the maximal rate of change of  $y_{\rm cap}$  and serves as a detection-of-

TABLE III
SUMMARY OF RMSE OF ESTIMATED TILTING ANGLE

	SNR 85	SNR 22	SNR 5	SNR 1	Overall
EKF $\theta_{RMSE}$	0.0050	0.0029	0.0026	0.0025	0.0034
HYB $\theta_{RMSE}$	0.0047	0.0023	0.0019	0.0018	0.0029
$\theta_{RMSE}$ reduced	6.9%	21.4%	27.6%	30.3%	15.1%
EKF $\theta_{RMSE,th}$	0.0055	0.0051	0.0050	0.0049	0.0051
HYB $\theta_{RMSE,th}$	0.0041	0.0045	0.0049	0.0045	0.0045
$\theta_{RME,th}$ reduced	26.0%	11.6%	2.6%	8.1%	12.3%

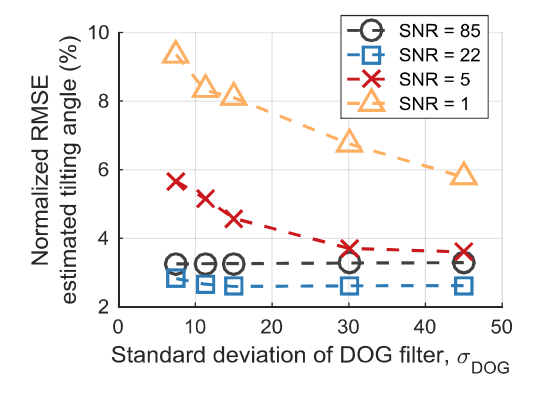


Fig. 10. Normalized RMSE with different SNR and various  $\sigma_{\rm DOG}$  settings. Under noisy condition (low SNR), increasing  $\sigma_{\rm DOG}$  effectively increases threshold detection accuracy and, therefore, increases state estimation accuracy of the EKF.

threshold-angle crossing. The four snapshots demonstrate that the detection method is robust under various SNR conditions.

Root mean square error (RMSE) of tilting angle  $\theta_{\rm RMSE}$  is defined as a performance metric

$$\theta_{\text{RMSE}} = \sqrt{\frac{1}{N} \sum_{i=1}^{N} \left(\hat{\theta}_i - \theta_{\text{PSD}, i}\right)^2}$$
 (14)

where  $\widehat{\theta_i}$  is a posteriori estimate of tilting angle and  $\theta_{\mathrm{PSD},i}$  is the tilting angle measured by the PSD at the *i*th sampling instance, and N is the number of sampling instants. A normalized RMSE (NRMSE) of tilting angle,  $\theta_{\mathrm{NRMSE}}$  is also defined and examined

$$\theta_{\text{NRMSE}} = \frac{\theta_{\text{RMSE}}}{\bar{\theta}_{\text{amp}}} \tag{15}$$

where  $\bar{\theta}_{\rm amp}$  is the average amplitude of the corresponding waveforms.  $\theta_{\rm RMSE}$  and  $\theta_{\rm NRMSE}$  are evaluated for the overall trajectories as well as each segment.

To evaluate the improvement made by introducing threshold sensing to the EKF,  $\theta_{\rm RMSE}$  within each segment of estimation trajectory generated by the two estimators are computed. Here,  $\theta_{\rm RMSE,th}$  denotes the RMSE computed using 50 sample points after each threshold has detection occurred. The results are listed in Table III.

From Table III, we can see that the reduction of RMSE by HYB over EKF are tabulated and bolded in Table III (third and sixth row) to quantify the estimation accuracy improvement thanks to the use of threshold position measurement, and the largest percentage improvement of total RMSE happens with SNR = 1. The largest improvement of RMSE after threshold detection location happens with SNR = 85. The result shows

that the threshold sensing adds the greatest local accuracy in high SNR conditions, but is more beneficial for overall EKF performance when SNR is low.

The trend of  $\theta_{\rm NRMSE}$  of each segment with respect to different  $\sigma_{\rm DOG}$  is shown in Fig. 10. For segments with high SNR (85 and 22), the change of  $\sigma_{\rm DOG}$  does not significantly change  $\theta_{\rm NRMSE}$ . However, for segments with low SNR (5 and 1), the analysis shows that increasing  $\sigma_{\rm DOG}$  significantly reduces  $\theta_{\rm NRMSE}$ , which suggests that the performance of EKF with threshold sensing is sensitive to selection of  $\sigma_{\rm DOG}$ .

# VII. CONCLUSION

In this paper, we introduced a method for utilizing a first-order DOG operator to detect threshold crossing from noisy signal and integrated this detection mechanism into an EKF to estimate states from a nonlinear process. To verify the effectiveness of the method, experimental and simulation studies were conducted to estimate the tilting angle of an electrostatic microscanner, and quantify various factors that might affect the error of threshold detection and EKF performance. Simulation showed that, first, an optimal sampling frequency exists for a minimal variance of detection timing error; second, increasing  $G_{\rm cap}(\theta)$  around threshold angle reduced variance of detection error in timing and angle, beneficial for improving an EKF accuracy.

Experimental results showed that use of the threshold-sensing mechanism improved the EKF performance across SNR conditions on an MEMS microscanner, with best improvement of a 30.3% reduction in RMSE of tilting angle estimation. On average, using threshold sensing improved the RMSE by 15.1% across a range of SNR scenarios. A sweep of width  $\sigma_{\rm DOG}$  of the DOG filter also showed that for low SNR, threshold detection accuracy was more sensitive to DOG filter parameter such as  $\sigma_{\rm DOG}$  and, therefore, needs to be selected carefully so that EKF can maximize the performance improvement of using the DOG filter.

# ACKNOWLEDGMENT

The authors would like to thank M. Birla for his help in taking SEM images of the device.

#### REFERENCES

- [1] A. J. Fleming, "A review of nanometer resolution position sensors: Operation and performance," *Sensors Actuators A, Phys.*, vol. 190, no. 1, pp. 106–126, Feb. 2013.
- [2] D. K. Shaeffer, "MEMS inertial sensors: A tutorial overview," *IEEE Commun. Mag.*, vol. 51, no. 4, pp. 100–109, Apr. 11, 2013.
- [3] Y. Chen, E. E. Aktakka, J.-K. Woo, K. Najafi, and K. R. Oldham, "On-chip capacitive sensing and tilting motion estimation of a microstage for in situ MEMS gyroscope calibration," *Mechatronics*, vol. 56, pp. 242–253, 2018.
- [4] P. R. Scheeper, A. V. D. Donk, W. Olthuis, and P. Bergveld, "A review of silicon microphones," *Sensors Actuators A, Phys.*, vol. 44, no. 1, pp. 1–11, 1994.
- [5] W. P. Eaton and J. H. Smith, "Micromachined pressure sensors: Review and recent developments," *Smart Mater. Struct.*, vol. 6, no. 5, 1997, Art. no. 530.
- [6] C. Acar and A. Shkel, MEMS Vibratory Gyroscopes: Structural Approaches to Improve Robustness. Berlin, Germany: Springer, 2008.
- [7] G. Stemme, "Resonant silicon sensors," J. Micromech. Microeng., vol. 1, no. 2, 1991, Art. no. 113.

- [8] Y. Chen and K. R. Oldham, "Kalman filter estimation with edge detection-based hybrid sensing," in *Proc. Amer. Control Conf.*, Boston, MA, USA, 2016, pp. 4526–4531.
- [9] T. Henningsson and K. J. Åström, "Log-concave observers," in *Proc. Math. Theory Netw. Syst.*, Kyoto, Japan, 2006, pp. 2163–2170.
- [10] Y. Chen, E. E. Aktakka, J.-K. Woo, and K. Oldham, "Threshold sensing signal construction from a capacitive sensor for MEMS gyroscope calibration," in *Proc. IEEE Int. Conf. Adv. Intell. Mechatronics*, Banff, AB, Canada, 2016, pp. 999–1004.
- [11] B. Edamana, Y. Chen, D. Slavin, E. E. Akatakka, and K. R. Oldham, "Estimation with threshold sensing for gyroscope calibration using a piezoelectric microstage," *IEEE Trans. Control Syst. Technol.*, vol. 23, no. 5, pp. 1943–1951, Sep. 2015.
- [12] H. Schenk *et al.*, "Large deflection micromechanical scanning mirrors for linear scans and pattern generation," *IEEE J. Sel. Topics Quantum Electron.*, vol. 6, no. 5, pp. 715–722, Sep./Oct. 2000.
- [13] H. Li *et al.*, "Integrated monolithic 3-D MEMS scanner for switchable real time vertical/horizontal cross-sectional imaging," *Opt. Express*, vol. 24, no. 3, pp. 2145–2155, Feb. 2016.
- [14] W. Shahid, Z. Qiu, X. Duan, L. Haijun, T. D. Wang, and R. K. Oldham, "Modeling and simulation of a parametrically resonant micromirror with duty-cycled excitation," *J. Microelectromech. Syst.*, vol. 23, no. 6, pp. 1440–1453, 2014.
- [15] N. Yazdi, H. Kulah, and K. Najafi, "Precision readout circuits for capacitive microaccelerometers," in *Proc. IEEE Sensors*, Vienna, Austria, 2004, pp. 28–31.
- [16] M. Basu, "Gaussian-based edge-detection methods—A survey," *IEEE Trans. Syst., Man, Cybern. C, Appl. Rev.*, vol. 32, no. 3, pp. 252–260, Aug. 2002.
- [17] J. Canny, "A computational approach to edge detection," *IEEE Trans. Pattern Anal. Mach. Intell.*, vol. PAMI-8, no. 6 pp. 679–698, Jun. 1986.
- [18] S. T. Holmstrom, U. Baran, and H. Urey, "MEMS Laser scanners: A review," J. Microelectromech. Syst., vol. 23, no. 2, pp. 259–275, 2014.
- [19] R. Schroedter, M. Roth, K. Janschek, and T. Sandner, "Flatness-based open-loop and closed-loop control for electrostatic quasi-static microscanners using jerk-limited trajectory design," *Mechatronics*, vol. 56, pp. 318– 331, 2018.
- [20] H. W. Lilliefors, "On the Kolmogorov-Smirnov test for normality with mean and variance unknown," *J. Amer. Stat. Assoc.*, vol. 62, no. 318, pp. 399–402, 1967.
- [21] S. Thrun, W. Burgard, and F. Dieter, *Probabilistic Robotics*. London, U.K.: MIT Press, 2005.
- [22] U. Hofmann, J. Janes, and H.-J. Quenzer, "High-Q MEMS resonators for laser beam scanning displays," *Micromachines*, vol. 3, no. 2, pp. 509–528, 2012



**Haijun Li** received the Ph.D. degree in microelectronics and solid-state electronics from Jilin University, Changchun, China, in 2007.

He held a Postdoctoral position with Nanyang Technology University, Singapore, from 2008 to 2011. He was a Senior Engineer with Hebei Semiconductor Research Institute, Shijiazhuang, China, from 1997 to 2008. He is currently a Research Investigator with the University of Michigan, Ann Arbor, MI, USA, where he is involved in the development of mi-

croelectromechanical system (MEMS) based endomicroscope. His research interests include MEMS, uncooled infrared detectors, epi-MEMS technology, and wafer-level packaging technologies.



Zhen Qiu was born in Wuhu, Anhui, China. He received the B.S. degree in precision instrumentation from the Department of Precision Instruments, Tsinghua University, Beijing, China, in 2004, and the Ph.D. degree in bio-optics and imaging from the Department of Biomedical Engineering, University of Michigan, Ann Arbor, MI, USA, in 2013.

He finished his postdoctoral training from the Department of Radiology and Molecular Imaging Program Stanford, School of Medicine, Stanford

University, CA, USA. He is currently an Assistant Professor with the Department of Biomedical Engineering, Institute for Quantitative Health Science and Engineering, Michigan State University, East Lansing, MI, USA. His research interests include biomedical optics, micro-electromechanical system and micro-opto-electro-mechanical system, multimodal targeted imaging using novel contrast agents, wearable, and implantable medical devices, ultrafast laser applications.

Prof. Qiu is a member of SPIE and OSA.



Thomas D. Wang received the B.S. degree in mathematics and physics from Harvey Mudd College, Claremont, CA, USA, in 1985, and the Ph.D. degree in medical engineering and medical physics from the Massachusetts Institute of Technology, Cambridge, MI, USA, in 1996.

He is currently a Professor of Medicine, Biomedical Engineering, and Mechanical Engineering with the University of Michigan, Ann Arbor, MI, USA, and the H. Marvin Pollard Collegiate Professor of Endoscopy Research. He

has developed a number of microsystem-based technologies to perform scanning and actuation for high-speed imaging with large working distance in endomicroscopy. His research interests include biomedical optics, multiplexed detection, and molecular imaging.



Yi Chen received the B.S. degrees in mechanical engineering from the University of Michigan, Ann Arbor, MI, USA, and Shanghai Jiao Tong University, Shanghai, China, in 2010, the master's degree in mechanical engineering, and another master's degree in electrical engineering and the Ph.D. degree in mechanical engineering from the University of Michigan, in 2012 and 2018, respectively.

He is currently a Software Engineer with Midea Emerging Technology Center, San Jose,

CA, USA. His research interests include signal processing, computer vision, and robotics.



**Kenn R. Oldham** (M'19) received the B.S. degree in mechanical engineering from Carnegie Mellon University, Pittsburgh, PA, USA, in 2000, and the Ph.D. degree in mechanical engineering from the University of California at Berkeley, Berkeley, CA, USA, in 2006.

He is currently an Associate Professor of Mechanical Engineering with the University of Michigan, Ann Arbor, MI, USA. His research focuses on the intersection of control systems and microscale sensing and actuation, with interests

in design for controllability, optimal and robust control, microsystem estimation and identification, and novel sensor and actuator design, including applications in terrestrial microrobotics, endoscopic microscopy, and inertial and physiological sensing.

Prof. Oldham is a member of ASME and IEEE.